

Cite this: DOI: 10.1039/xxxxxxxxxx

Photogenerated Electron-Hole Plasma Induced Symmetry Breaking in Spherical Silicon Nanoparticle

Anton Rudenko,^{*a} Konstantin Ladutenko,^b Sergey Makarov^b and Tatiana E. Itina^{ab}

^a Laboratoire Hubert Curien, UMR CNRS 5516, University of Lyon/UJM, 42000, Saint-Etienne, France ^b ITMO University, Kronverksiy pr. 49, Saint-Petersburg, Russia

Received Date

Accepted Date

DOI: 10.1039/xxxxxxxxxx

www.rsc.org/journalname

The concept of nonlinear all-dielectric nanophotonics based on high refractive index (e.g., silicon) nanoparticles supporting magnetic optical response has recently emerged as a powerful tool for ultrafast all-optical modulation at nanoscale. A strong modulation can be achieved via photo-generation of dense electron-hole plasma in the regime of simultaneous excitation of electric and magnetic Mie resonances, resulting in an effective transient reconfiguration of nanoparticle scattering properties. However, only homogeneous plasma generation was previously considered in a photo-excited nanoparticle, remaining unexplored any effects related to the plasma-induced optical inhomogeneities. Here we examine these effects by using 3D numerical modeling of coupled electrodynamic and material ionization equations. Based on the simulation results, we observed a deeply subwavelength plasma-induced nanopatterning of spherical silicon nanoparticles. In particular, we revealed strong symmetry breaking in the initially symmetrical nanoparticle, which arises during ultrafast photoexcitation near the magnetic dipole resonance. The proposed ultrafast breaking of the nanoparticle symmetry paves the way to the novel opportunities for nonlinear optical nanodevices.

1 Introduction

All-dielectric nonlinear nanophotonics based on high refractive index dielectric materials has become prospective paradigm in modern optics, owing to recent advances in harmonics generation^{1–6} and ultrafast all-optical modulation^{2,7–12}. In fact, all-dielectric nanoantennas and metasurfaces possess much smaller parasitic Joule losses at high intensities as compared with their plasmonic counterparts, whereas their nonlinear properties are comparable. More importantly, the unique properties of nonlinear all-dielectric nanodevices are due to the existence of both electric and magnetic optical resonances in visible and near IR ranges¹³. For instance, even slight variation of dielectric permittivity around optical resonances leads to significant changes in optical properties (transmittance or reflectance) of all-dielectric nanoantennas^{8,10,11} and metasurfaces^{2,7,9,12}.

In previous works on all-dielectric nonlinear nanostructures, the building blocks (nanoparticles) were considered as objects with dielectric permittivity *homogeneously* distributed over nanoparticle (NP). Therefore, in order to manipulate the propa-

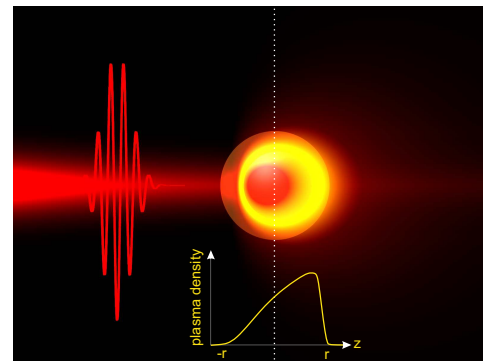


Fig. 1 Schematic illustration of electron-hole plasma 2D and 1D distributions in silicon nanoparticle around a magnetic resonance.

gation angle of the transmitted light it was proposed to use complicated nanostructures with reduced symmetry^{11,14,15}. On the other hand, plasma explosion imaging technique¹⁶ revealed *in situ* strongly asymmetrical electron-hole plasma (EHP) distribution in various dielectric NPs during their pumping by femtosecond laser pulses. Therefore, local permittivity in the strongly photoexcited NPs can be significantly inhomogeneous, and symmetry

^a Univ Lyon, UJM-St-Etienne, CNRS UMR 5516, F-42000, Saint-Etienne, France
^b ITMO University, Kronverksiy pr. 49, St. Petersburg, Russia

of nanoparticles can be reduced.

In this Letter, we show theoretically that ultra-fast photo-excitation in a spherical silicon NP leads to a strongly inhomogeneous EHP distribution, as is shown schematically in Fig. 1. To reveal and analyze this effect, we perform a full-wave numerical simulation. We consider an intense femtosecond (fs) laser pulse to interact with a silicon NP supporting Mie resonances and two-photon EHP generation. In particular, we couple finite-difference time-domain (FDTD) method used to solve three-dimensional Maxwell equations with kinetic equations describing nonlinear EHP generation. Three-dimensional transient variation of the material dielectric permittivity is calculated for NPs of several sizes. The obtained results propose a novel strategy to create complicated non-symmetrical nanostructures by using single photo-excited spherical silicon NPs. Moreover, we show that a dense EHP can be generated at deeply subwavelength scale ($< \lambda/10$) supporting the formation of small metalized parts inside the NP. In fact, such effects transform a dielectric NP to a hybrid metall-dielectric one strongly extending functionality of the ultra-fast optical nanoantennas.

2 Modeling details

We focus attention on silicon because this material is promising for the implementation of numerous nonlinear photonic devices. This advantage is based on a broad range of optical nonlinearities, strong two-photon absorption, as well as a possibility of the photo-induced EHP excitation¹⁷. Furthermore, silicon nanoantennas demonstrate a sufficiently high damage threshold due to the high melting temperature (≈ 1690 K), whereas its nonlinear optical properties were extensively studied during the last decades^{17–19}. High silicon melting point typically preserves structures formed from this material up to the EHP densities on the order of the critical value²⁰ $N_{cr} \approx 5 \cdot 10^{21}$ cm⁻³. At the critical density and above, silicon acquires metallic properties ($Re(\epsilon) < 0$) and contributes to the EHP reconfiguration during ultrashort laser irradiation.

The process of three-dimensional photo-generation and temporal evolution of EHP in silicon NPs has not been modeled before. Therefore, herein we propose a model considering ultra-short laser interactions with a resonant silicon sphere, where the EHP is generated via one- and two-photon absorption processes. Importantly, we also consider nonlinear feedback of the material by taking into account the intraband light absorption on the generated free carriers. To simplify our model, we neglect free carrier diffusion due to the considered short time scales. In fact, the aim of the present work is to study the EHP dynamics *during* ultra-short (fs) laser interaction with the NP. The created electron-hole modifies both laser-particle interaction and, hence, the following particle evolution. However, the plasma then will recombine at picosecond time scale.

2.1 Light propagation

The incident wave propagates in positive direction of z axis, the NP geometric center located at $z = 0$ front side corresponds to the volume $z > 0$ and back side for $z < 0$, as shown in Fig. 1.

Ultra-short laser interaction and light propagation inside the silicon NP are modeled by solving the system of three-dimensional Maxwell's equations written in the following way

$$\begin{cases} \frac{\partial \vec{E}}{\partial t} = \frac{\nabla \times \vec{H}}{\epsilon_0 \epsilon} - \frac{1}{\epsilon_0 \epsilon} (\vec{J}_p + \vec{J}_{Kerr}) \\ \frac{\partial \vec{H}}{\partial t} = -\frac{\nabla \times \vec{E}}{\mu_0}, \end{cases} \quad (1)$$

where \vec{E} is the electric field, \vec{H} is the magnetizing field, ϵ_0 is the free space permittivity, μ_0 is the permeability of free space, $\epsilon = n^2 = 3.681^2$ is the permittivity of non-excited silicon at 800 nm wavelength²¹, \vec{J}_p and \vec{J}_{Kerr} are the nonlinear currents, which include the contribution due to Kerr effect $\vec{J}_{Kerr} = \epsilon_0 \epsilon_\infty \chi_3 \frac{\partial (|\vec{E}|^2 \vec{E})}{\partial t}$, where $\chi_3 = 4 \cdot 10^{-20}$ m²/V² for laser wavelength $\lambda = 800$ nm²², and heating of the conduction band, described by the differential equation derived from the Drude model

$$\frac{\partial \vec{J}_p}{\partial t} = -v_e \vec{J}_p + \frac{e^2 N_e(t)}{m_e^*} \vec{E}, \quad (2)$$

where e is the elementary charge, $m_e^* = 0.18m_e$ is the reduced electron-hole mass¹⁹, $N_e(t)$ is the time-dependent free carrier density and $v_e = 10^{15}$ s⁻¹ is the electron collision frequency¹⁹. Silicon NP is surrounded by vacuum, where the light propagation is calculated by Maxwell's equations with $\vec{J} = 0$ and $\epsilon = 1$. The system of Maxwell's equations coupled with electron density equation is solved by the finite-difference numerical method²³, based on the finite-difference time-domain (FDTD)²⁴ and auxiliary-differential methods for dispersive media²⁵. At the edges of the grid, we apply the absorbing boundary conditions related to convolutional perfectly matched layers to avoid nonphysical reflections²⁶. The initial electric field is introduced as a Gaussian slightly focused beam as follows

$$E_x(t, r, z) = \frac{w_0}{w(z)} \exp \left(i\omega t - \frac{r^2}{w(z)^2} - ikz - ik \frac{r^2}{2R(z)} + i\zeta(z) \right) \times \exp \left(-\frac{4 \ln 2(t-t_0)^2}{\theta^2} \right), \quad (3)$$

where $\theta \approx 130$ fs is the temporal pulse width at the half maximum (FWHM), t_0 is the time delay, $w_0 = 3\mu\text{m}$ is the beam waist, $w(z) = w_0 \sqrt{1 + (\frac{z}{z_R})^2}$ is the Gaussian's beam spot size, $\omega = 2\pi c/\lambda$ is the angular frequency, $\lambda = 800$ nm is the laser wavelength in air, c is the speed of light, $z_R = \frac{\pi w_0^2 n_0}{\lambda}$ is the Rayleigh length, $r = \sqrt{x^2 + y^2}$ is the radial distance from the beam's waist, $R_z = z(1 + (\frac{z}{z_R})^2)$ is the radius of curvature of the wavelength comprising the beam, and $\zeta(z) = \arctan(\frac{z}{z_R})$ is the Gouy phase shift.

2.2 Material ionization

To account for the material ionization induced by a sufficiently intense laser field inside the particle, we couple Maxwell's equations with the kinetic equation for the electron-hole plasma as described below.

The time-dependent conduction-band carrier density evolution is described by the rate equation proposed by van Driel¹⁸. This

equation takes into account such processes as photoionization, avalanche ionization and Auger recombination, and is written as

$$\frac{dN_e}{dt} = \frac{N_a - N_e}{N_a} \left(\frac{\sigma_1 I}{\hbar\omega} + \frac{\sigma_2 I^2}{2\hbar\omega} \right) + \alpha IN_e - \frac{C \cdot N_e^3}{C\tau_{rec}N_e^2 + 1}, \quad (4)$$

where $I = \frac{n}{2} \sqrt{\frac{\epsilon_0}{\mu_0}} |\vec{E}|^2$ is the intensity, $\sigma_1 = 1.021 \cdot 10^3 \text{ cm}^{-1}$ and $\sigma_2 = 0.1 \cdot 10^{-7} \text{ cm/W}$ are the one-photon and two-photon interband cross-sections^{22,27,28}, $N_a = 5 \cdot 10^{22} \text{ cm}^{-3}$ is the particle saturation density²⁸, $C = 3.8 \cdot 10^{-31} \text{ cm}^6/\text{s}$ is the Auger recombination rate¹⁸, $\tau_{rec} = 6 \cdot 10^{-12} \text{ s}$ is the minimum Auger recombination time²⁹, and $\alpha = 21.2 \text{ cm}^2/\text{J}$ is the avalanche ionization coefficient³⁰ at the wavelength 800 nm in air. As we have noted, free carrier diffusion is neglected during and shortly after the laser excitation^{18,19}. In particular, from the Einstein formula $D = k_B T_e \tau / m^* \approx (1-2) \cdot 10^{-3} \text{ m}^2/\text{s}$ (k_B is the Boltzmann constant, T_e is the electron temperature, $\tau = 1 \text{ fs}$ is the collision time, $m^* = 0.18m_e$ is the effective mass), where $T_e \approx 2 \cdot 10^4 \text{ K}$ for N_e close to N_{cr} ³¹. It means that during the pulse duration ($\approx 130 \text{ fs}$) the diffusion length will be around 10–15 nm for N_e close to N_{cr} .

The changes of the real and imaginary parts of the permittivity associated with the time-dependent free carrier response¹⁹ can be derived from equations (1, 2) and are written as follows

$$\begin{cases} Re(\epsilon^*) = \epsilon - \frac{e^2 N_e}{\epsilon_0 m_e^* (\omega^2 + v_e^2)} \\ Im(\epsilon^*) = \frac{e^2 N_e v_e}{\epsilon_0 m_e^* \omega (\omega^2 + v_e^2)}. \end{cases} \quad (5)$$

2.3 Mie calculations

A steady-state interaction of a plain electromagnetic wave with a spherical particle has a well-known analytical solution described by a Mie theory³². It is only valid in the absence of nonlinear optical response, thus we can compare it against above-mentioned FDTD-EHP model only for small plasma densities, where we can neglect EHP impact to the refractive index. Non-stationary nature of a fs pulse increases the complexity of the analysis. A detailed discussion on the relation between the Mie theory and FDTD-EHP model will be provided in the next section.

We used the Scattnlay program to evaluate calculations of Lorentz-Mie coefficients (a_i , b_i) and near-field distribution³³. This program is available online at GitHub³⁴ under open source license.

3 Results and discussion

3.1 Asymmetry factors

We start with a pure electromagnetic problem without EHP generation. We plot in Fig. 2(a) Mie coefficients of a Si NP as a function of its size for a fixed laser wavelength $\lambda = 800 \text{ nm}$. For the NP sizes under consideration most of contribution to the electromagnetic response originates from electric and magnetic dipole (ED and MD), while for sizes near $R \approx 150 \text{ nm}$ a magnetic quadrupole (MQ) response turns to be the main one. The superposition of multipoles defines the distribution of electric field inside the NP. We introduce G_I factor of asymmetry, corresponding to difference between the volume integral of squared electric field in the

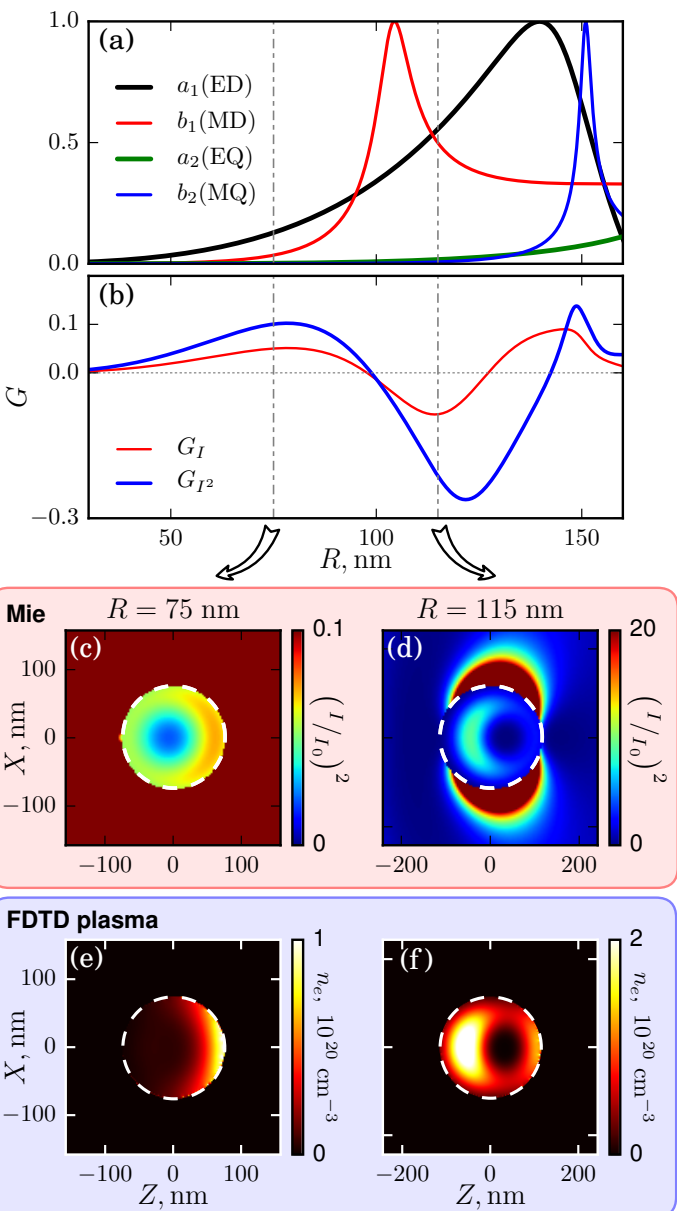


Fig. 2 (a) First four Lorentz-Mie coefficients (a_1 , a_2 , b_1 , b_2) and (b) factors of asymmetry G_I , G_{I^2} according to the Mie theory at fixed wavelength 800 nm. (c, d) Squared intensity distributions at different radii R calculated by the Mie theory and (e, f) EHP distribution for low densities $N_e \approx 10^{20} \text{ cm}^{-3}$ by Maxwell's equations (1, 2) coupled with EHP density equation (4). (c-f) Incident light propagates from the left to the right along Z axis, electric field polarization \vec{E} is along X axis.

front side (I^{front}) of the NP to that in the back side (I^{back}) normalized to their sum: $G_I = (I^{front} - I^{back})/(I^{front} + I^{back})$, where $I^{front} = \int_{(z>0)} |E|^2 dv$ and $I^{back} = \int_{(z<0)} |E|^2 dv$ are expressed via amplitude of the electric field $|E|$. The factor G_{I^2} was determined in a similar way by using volume integrals of squared intensity to predict EHP asymmetry due to two-photon absorption. Fig. 2(b) shows G factors as a function of the NP size. For the NPs of sizes below the first MD resonance, the intensity is enhanced in the front side as in Fig. 2(c) and $G_I > 0$. The behavior changes near the size resonance value, corresponding to $R \approx 105 \text{ nm}$. In con-

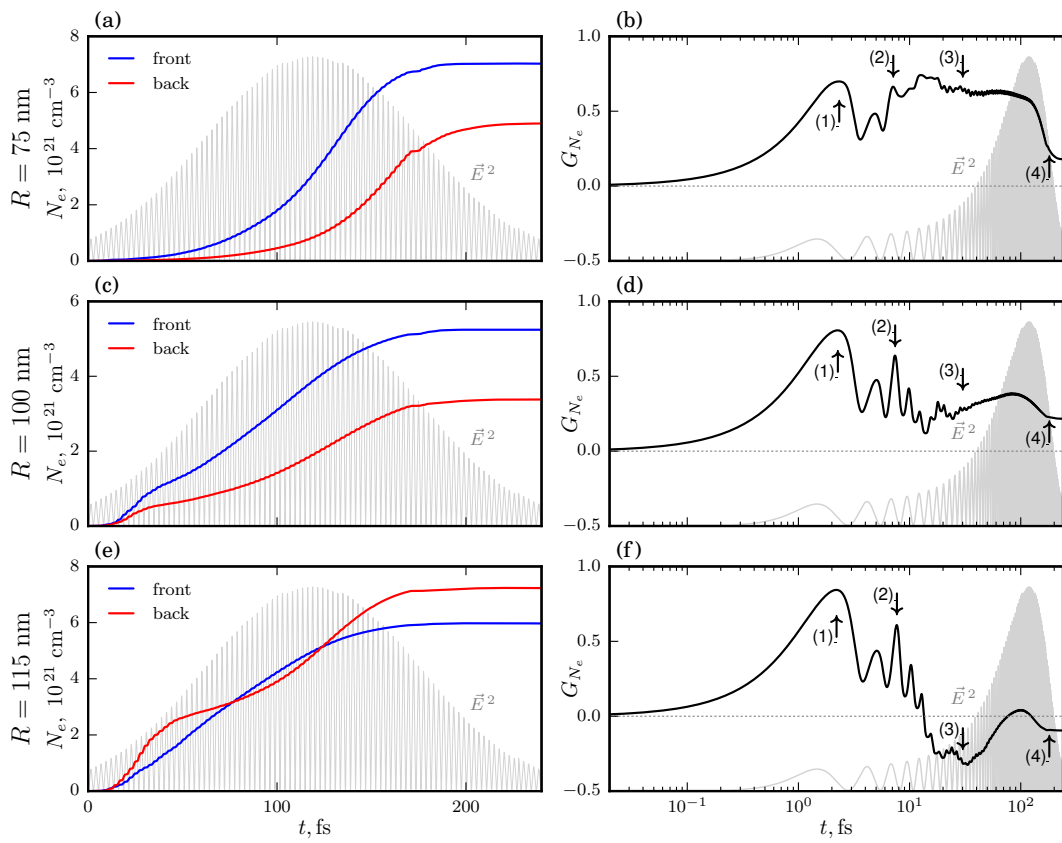


Fig. 3 Temporal EHP (a, c, e) and asymmetry factor G_{N_e} (b, d, f) evolution for different Si nanoparticle radii of (a, b) $R = 75 \text{ nm}$, (c, d) $R = 100 \text{ nm}$, and (e, f) $R = 115 \text{ nm}$. Pulse duration 130 fs (FWHM). Wavelength 800 nm in air. (b, d, f) Different stages of EHP evolution shown in Fig. 4 are indicated. The temporal evolution of Gaussian beam intensity is also shown. Peak laser intensity is fixed to be 10^{12} W/cm^2 . For better visual representation of time scale at a single optical cycle we put a squared electric field profile in all plots in Fig. 3 in gray color as a background image (note linear time scale on the left column and logarithmic scale on the right one).

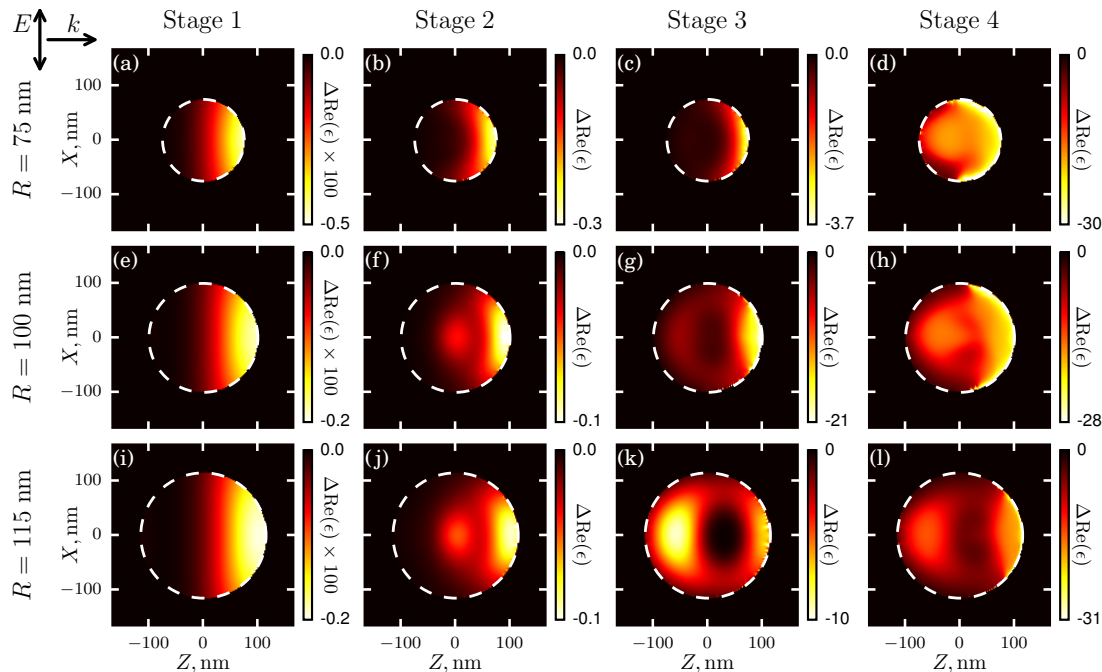


Fig. 4 EHP density snapshots inside Si nanoparticle of radii $R = 75 \text{ nm}$ (a-d), $R = 100 \text{ nm}$ (e-h) and $R = 115 \text{ nm}$ (i-l) taken at different times and conditions of excitation (stages 1–4: (1) first optical cycle, (2) maximum during few optical cycles, (3) quasi-stationary regime, (4) strongly nonlinear regime). $\Delta \text{Re}(\epsilon)$ indicates the real part change of the local permittivity defined by Equation (5). Pulse duration 130 fs (FWHM). Wavelength 800 nm in air. Peak laser intensity is fixed to be 10^{12} W/cm^2 .

trast, for larger sizes, the intensity is enhanced in the back side of the NP as demonstrated in Fig. 2(d). In fact, rather similar EHP distributions can be obtained by applying Maxwell's equations coupled with the rate equation for a relatively weak excitation with EHP concentration of $N_e \approx 10^{20} \text{ cm}^{-3}$, see Fig. 2(e,f). The optical properties do not change considerably due to the excitation according to (5). Therefore, the excitation processes follow the intensity distribution. However, such coincidence was achieved under quasi-stationary conditions, after the electric field made enough oscillations inside the Si NP. Further on, we present transient analysis, which reveals much more details.

To achieve a quantitative description for evolution of the EHP distribution during the *fs* pulse, we introduced another asymmetry factor $G_{N_e} = (N_e^{\text{front}} - N_e^{\text{back}})/(N_e^{\text{front}} + N_e^{\text{back}})$ indicating the relationship between the average EHP densities in the front and in the back halves of the NP, defined as $N_e^{\text{front}} = \frac{2}{V} \int_{(z>0)} N_e dv$ and $N_e^{\text{back}} = \frac{2}{V} \int_{(z<0)} N_e dv$, where $V = \frac{4}{3}\pi R^3$ is the volume of the nanosphere. In this way, $G_{N_e} = 0$ corresponds to the symmetrical case and the assumption of the NP homogeneous EHP distribution can be made to investigate the optical response of the excited Si NP. When G_{N_e} significantly differs from 0, this assumption, however, could not be justified. In what follows, we discuss the results of the numerical modeling of the temporal evolution of EHP densities and the asymmetry factors G_{N_e} for different sizes of Si NP, as shown in Fig. 3. Typical change in permittivity corresponding to each stage is shown in Fig. 4. It reveals the EHP evolution stages during interaction of femtosecond laser pulse with the Si NPs.

3.2 Stages of transient Si nanoparticle photoexcitation

To describe all the stages of non-linear light interaction with Si NP, we present the calculation results obtained by using Maxwell's equations coupled with electron kinetics equations for different radii for resonant and non-resonant conditions at peak intensity 10^{12} W/cm^2 and $\lambda = 800 \text{ nm}$. In this case, the geometry of the EHP distribution can strongly deviate from the intensity distribution given by the Mie theory. Two main reasons cause the deviation: (i) non-stationarity of interaction between electromagnetic pulse and NP (ii) nonlinear effects, taking place due to transient optical changes in Si. The non-stationary intensity deposition during *fs* pulse results in different time delays for exciting electric and magnetic resonances inside Si NP because of different quality factors Q of the resonances. In particular, MD resonance (*b1*) has $Q \approx 8$, whereas electric one (*a1*) has $Q \approx 4$. The larger particle supporting MQ resonance (*b2*) demonstrates $Q \approx 40$. As soon as the electromagnetic wave period at $\lambda = 800 \text{ nm}$ is $\approx 2.7 \text{ fs}$, one needs about 10 fs to pump the ED, 20 fs for the MD, and about 100 fs for the MQ. According to these considerations, after few optical cycles taking place on a 10 fs scale it results in the excitation of the low- Q ED resonance, which dominates MD and MQ independently on the exact size of NPs. Moreover, during the first optical cycle there is no multipole modes structure inside NP, which results in a very similar field distribution for all sizes of NP under consideration as shown in Fig. 4(a,e,i). We address to this phenomena as '*Stage 1*'. This stage demonstrates the initial penetration of electromagnetic field into the NP during the

first optical cycle. Resulting factors G_{N_e} exhibit sharp increase at this stage (Fig. 3(b,d,f)), yielding strong and ultrafast symmetry breaking.

'*Stage 2*' corresponds to further electric field oscillations ($t \approx 5\text{--}15 \text{ fs}$) leading to the formation of ED E-field pattern in the center of the Si NP as shown in Fig. 4(f,j). We stress the nonstationary nature of E-field pattern at this stage, whereas there is a simultaneous growth of the incident pulse amplitude. This leads to a superposition of ED near-field pattern with that from Stage 1, resulting in EHP concentration in the front side of the Si NP. This effect dominates for the smallest NP with $R = 75 \text{ nm}$ in Fig. 4(b), where ED mode is tuned far away from the resonance (see Fig. 2(c) for field suppression inside NP predicted by the Mie theory). At this stage, the density of EHP ($N_e < 10^{20} \text{ cm}^2$) is still not high enough to significantly affect the optical properties of the NP (Figs. 3(a,c,e)).

When the number of optical cycles is large enough ($t > 20 \text{ fs}$) both ED and MD modes can be exited to the level necessary to achieve the stationary intensity pattern corresponding to the Mie-based intensity distribution at '*Stage 3*' (see Fig. 4(c,g,k)). The EHP density for the most volume of NP is still relatively small to affect the EHP evolution, but is already high enough to change the local optical properties, i.e. real part of permittivity. Below the MD resonance ($R = 75 \text{ nm}$), the EHP is mostly localized in the front side of the NP as shown in Fig. 4(c). The highest quasi-stationary asymmetry factor $G_{N_e} \approx 0.5\text{--}0.6$ is achieved in this case (Fig. 3(b)). At the MD resonance conditions ($R = 100 \text{ nm}$), the EHP distribution has a toroidal shape and is much closer to the homogeneous distribution. In contrast, above the MD resonant size for $R = 115 \text{ nm}$ the $G_{N_e} < 0$ due to the fact that EHP is dominantly localized in the back side of the NP.

Due to a quasi-stationary pumping during Stage 3, it is superposed with Stage 1 field pattern, resulting in an additional EHP localized in the front side. This can be seen when comparing result from the Mie theory in Fig. 2(d) with that of full 3D simulation in Fig. 2(f). Note that pumping of NP significantly changes during a single optical cycle, this leads to a large variation of asymmetry factor G_{N_e} at the first stage. This variation steadily decreases as it goes to Stage 3, as shown in Fig. 3(b,d,f).

To explain this effect, we consider the time evolution of average EHP densities N_e in the front and back halves of the NP presented in Fig. 3(a,c,e). As soon as the recombination and diffusion processes are negligible at *fs* time scale, both N_e^{front} and N_e^{back} curves experience monotonous behavior with small pumping steps synced to the incident pulse. The front and the back halves of NP are separated in space, which obviously leads to the presence of time delay between pumping steps in each curve caused by the same optical cycle of the incident wave. This delay causes a large asymmetry factor during the first stage. However, as soon as average EHP density increases, the relative contribution of these pumping steps to the resulting asymmetry becomes smaller. This way variations of asymmetry G_{N_e} synced with the period of incident light decrease.

Higher excitation conditions are followed by larger values of electric field amplitude, which leads to the appearance of high EHP densities causing a significant change in the optical proper-

ties of silicon according to the equations (5). From the Mie theory, the initial (at the end of Stage 3) spatial pattern of the optical properties is non-homogeneous. When non-homogeneity of the optical properties becomes strong enough it leads to the reconfiguration of the E-field inside NP, which in turn strongly affects further reconfiguration of the optical properties. We refer to these strong nonlinear phenomena as 'Stage 4'. In general, the reconfiguration of the electric field is unavoidable as far as the result from the Mie theory comes with the assumption of homogeneous optical properties in a spherical NP.

Thus, the evolution of EHP density during Stage 4 depends on the result of multipole modes superposition at the end of Stage 3 and is quite different as we change the size of NP. For $R = 75$ nm and $R = 100$ nm, we observe a front side asymmetry before Stage 4, however, its origin is quite different. The $R = 75$ nm NP is out of resonance, moreover, Mie field pattern and the one, which comes from Stage 1 are quite similar. As soon as EHP density becomes high enough to change optical properties, the NP is still out of resonance, however, the presence of EHP increases absorption in agreement with (5), decreases Q-factor, and destroys optical modes.

For $R = 100$ nm, the evolution during the final stage goes in a similar way, with a notable exception regarding MD resonance. As soon as presence of EHP increases the absorption, it suppresses the MD resonance with symmetric field pattern, thus, the asymmetry factor can be increased. This result was observed in Fig. 3(d) with a local maximum near 100 fs mark.

The last NP with $R = 115$ nm shows the most complex behavior during Stage 4. The superposition of Mie-like E-field pattern with that from Stage 1 results in the presence of two EHP spatial maxima, back and front shifted. They serve as starting seeds for the EHP formation, and an interplay between them forms a complex behavior of the asymmetry factor curve. Namely, the sign is changed from negative to positive and back during the last stage. This numerical result can hardly be explained in a simple qualitative manner, it is too complex to account all near-field interaction of incident light with two EHP regions inside a single NP. It is interesting to note, however, that in a similar way as it was for $R = 100$ nm the increased absorption should destroy ED and MD resonances, which are responsible for the back-shifted EHP. As soon as this EHP region is quite visible on the last snapshot in Fig. 4(l), this means that EHP seeds are self-supporting.

As the EHP acquires quasi-metallic properties at stronger excitation $N_e > 5 \cdot 10^{21} \text{ cm}^{-3}$, the EHP distribution evolves inside NPs because of the photoionization and avalanche ionization induced transient optical response and the effect of newly formed EHP. This way, the distribution becomes more homogeneous and the effect is likely to be enhanced by electron diffusion inside Si NPs.

It is worth noting that it is possible to achieve the formation of deeply subwavelength EHP regions due to high field localization. The smallest EHP localization and the larger asymmetry factor are achieved below the MD resonant conditions for $R < 100$ nm. Thus, the EHP distribution in Fig. 4(c) is optimal for symmetry breaking in Si NP, as it results in the larger asymmetry factor G_{N_e} and higher electron densities N_e . We stress here that such regime could be still safe for NP due to the very small volume where such

high EHP density is formed.

4 Conclusions

We have rigorously modeled and studied ultra-fast and intense light interaction with a single silicon nanoparticle of various sizes for the first time to our best knowledge. As a result of the presented self-consistent nonlinear calculations, we have obtained spatio-temporal EHP evolution inside the NPs and investigated the asymmetry of the EHP distributions. We have revealed EHP strong asymmetric distribution during the first optical cycle for different sizes. The highest average EHP asymmetry has been observed for NPs of smaller sizes below the first magnetic dipole resonance, when EHP is concentrated in the front side mostly during the laser pulse absorption. Essentially different EHP evolution and lower asymmetry has been achieved for larger NPs due to the intensity enhancement in the back side of the NP. The EHP densities above the critical value have been shown to lead to homogenization of the EHP distribution. The observed plasma-induced breaking symmetry can be useful for creation of nonsymmetrical nanophotonic designs, e.g. for beam steering or enhanced second harmonics generation. Also, the asymmetric EHP opens a wide range of applications in NP nanomachining at deeply subwavelength scale.

5 Acknowledgments

A. R. and T. E. I. gratefully acknowledge the CINES of CNRS for computer support. S. V. M. is thankful to ITMO Fellowship Program. This work was partially supported by Russian Foundation for Basic Researches (grants 17-03-00621, 17-02-00538, 16-29-05317).

References

- 1 M. R. Shcherbakov, D. N. Neshev, B. Hopkins, A. S. Shorokhov, I. Staude, E. V. Melik-Gaykazyan, M. Decker, A. A. Ezhov, A. E. Miroshnichenko, I. Brener *et al.*, *Nano Letters*, 2014, **14**, 6488–6492.
- 2 Y. Yang, W. Wang, A. Boulesbaa, I. I. Kravchenko, D. P. Briggs, A. Puretzky, D. Geohegan and J. Valentine, *Nano Letters*, 2015, **15**, 7388–7393.
- 3 S. Makarov, A. Tsypkin, T. Voytova, V. Milichko, I. Mukhin, A. Yulin, S. Putilin, M. Baranov, A. Krasnok, I. Morozov *et al.*, *Nanoscale*, 2016, **8**, 17809–17814.
- 4 A. S. Shorokhov, E. V. Melik-Gaykazyan, D. A. Smirnova, B. Hopkins, K. E. Chong, D.-Y. Choi, M. R. Shcherbakov, A. E. Miroshnichenko, D. N. Neshev, A. A. Fedyakin *et al.*, *Nano Letters*, 2016, **16**, 4857–4861.
- 5 S. V. Makarov, M. I. Petrov, U. Zywicki, V. Milichko, D. Zuev, N. Lopanitsyna, A. Kuksin, I. Mukhin, G. Zograf, E. Ubyivovik *et al.*, *Nano Letters*, 2017, **17**, 3047–3053.
- 6 S. V. Makarov, A. S. Zalogina, M. Tajik, D. A. Zuev, M. V. Rybin, A. A. Kuchmizhak, S. Juodkazis and Y. Kivshar, *Laser & Photonics Reviews*, 2017, doi: 10.1002/lpor.201700108.
- 7 P. P. Iyer, N. A. Butakov and J. A. Schuller, *ACS Photonics*, 2015, **2**, 1077–1084.
- 8 S. Makarov, S. Kudryashov, I. Mukhin, A. Mozharov,

- V. Milichko, A. Krasnok and P. Belov, *Nano Letters*, 2015, **15**, 6187–6192.
- 9 M. R. Shcherbakov, P. P. Vabishchevich, A. S. Shorokhov, K. E. Chong, D.-Y. Choi, I. Staude, A. E. Miroshnichenko, D. N. Neshhev, A. A. Fedyanin and Y. S. Kivshar, *Nano Letters*, 2015, **15**, 6985–6990.
- 10 D. G. Baranov, S. V. Makarov, V. A. Milichko, S. I. Kudryashov, A. E. Krasnok and P. A. Belov, *ACS Photonics*, 2016, **3**, 1546.
- 11 D. G. Baranov, S. V. Makarov, A. E. Krasnok, P. A. Belov and A. Alù, *Laser & Photonics Reviews*, 2016, **10**, 1009–1015.
- 12 M. R. Shcherbakov, S. Liu, V. V. Zubiyuk, A. Vaskin, P. P. Vabishchevich, G. Keeler, T. Pertsch, T. V. Dolgova, I. Staude, I. Brener *et al.*, *Nature Communications*, 2017, **8**, 1–6.
- 13 A. I. Kuznetsov, A. E. Miroshnichenko, M. L. Brongersma, Y. S. Kivshar and B. Luk'yanchuk, *Science*, 2016, **354**, aag2472.
- 14 P. Albella, T. Shibanuma and S. A. Maier, *Scientific Reports*, 2015, **5**, 1–8.
- 15 T. Shibanuma, P. Albella and S. A. Maier, *Nanoscale*, 2016, **8**, 14184–14192.
- 16 D. D. Hickstein, F. Dollar, J. L. Ellis, K. J. Schnitzenbaumer, K. E. Keister, G. M. Petrov, C. Ding, B. B. Palm, J. A. Gaffney, M. E. Foord *et al.*, *ACS Nano*, 2014, **8**, 8810–8818.
- 17 J. Leuthold, C. Koos and W. Freude, *Nature Photonics*, 2010, **4**, 535.
- 18 H. M. Van Driel, *Physical Review B*, 1987, **35**, 8166.
- 19 K. Sokolowski-Tinten and D. von der Linde, *Physical Review B*, 2000, **61**, 2643.
- 20 D. Korfiatis, K. T. Thoma and J. Vardaxoglou, *Journal of Physics D: Applied Physics*, 2007, **40**, 6803.
- 21 M. A. Green and M. J. Keevers, *Progress in Photovoltaics: Research and Applications*, 1995, **3**, 189–192.
- 22 A. D. Bristow, N. Rotenberg and H. M. Van Driel, *Appl. Phys. Lett.*, 2007, **90**, 191104.
- 23 A. Rudenko, J.-P. Colombier and T. E. Itina, *International Journal of Numerical Modelling: Electronic Networks, Devices and Fields*, 2016, e2215.
- 24 K. S. Yee, *IEEE Trans. Antennas and Propagation*, 1966, 302–307.
- 25 A. Taflove, S. C. Hagness *et al.*, *Norwood, 2nd Edition, MA: Artech House, 1995*, 1995.
- 26 J. A. Roden and S. D. Gedney, *Microwave and Optical Technology Letters*, 2000, **27**, 334–339.
- 27 T. Y. Choi and C. P. Grigoropoulos, *Journal of Applied Physics*, 2002, **92**, 4918–4925.
- 28 T. J.-Y. Derrien, T. E. Itina, R. Torres, T. Sarnet and M. Sentis, *Journal of Applied Physics*, 2013, **114**, 083104.
- 29 E. J. Yoffa, *Physical Review B*, 1980, **21**, 2415.
- 30 P. Pronko, P. VanRompay, C. Horvath, F. Loesel, T. Juhasz, X. Liu and G. Mourou, *Physical Review B*, 1998, **58**, 2387.
- 31 A. Rämer, O. Osmani and B. Rethfeld, *Journal of Applied Physics*, 2014, **116**, 053508.
- 32 C. F. Bohren and D. Huffman, *Absorption and scattering of light by small particles*, Wiley, 1983.
- 33 K. Ladutenko, U. Pal, A. Rivera and O. Peña-Rodríguez, *Computer Physics Communications*, 2017, **214**, 225 – 230.
- 34 <https://github.com/ovidiopr/scattnlay>.